Journal of ELECTRONIC MATERIALS, Vol. 45, No. 6, 2016
DOI: 10.1007/s11664-016-4472-y

Structural, Electrical and Dielectrical Property Investigations of Fe-Doped $BaZrO_3$ Nanoceramics

PANKAJ P. KHIRADE,[1,2] SHANKAR D. BIRAJDAR,[1] ASHOK V. HUMBE,[1] and K.M. JADHAV[1]

1.—Department of Physics, Dr. Babasaheb Ambedkar Marathwada University, Aurangabad, MS, India. 2.—e-mail: pankajkhirade@gmail.com

Nanocrystalline samples of $BaZr_{1-x}Fe_xO_3$ (x = 0.0, 0.05, 0.10, 0.20, 0.30, 0.40 and 0.50) ceramics were synthesized by the wet chemical sol–gel auto combustion method. The perovskite structured cubic phase formation of $BaZr_{1-x}Fe_xO_3$ samples was confirmed by x-ray diffraction (XRD) data analysis. Various structural parameters such as lattice constant (a), unit cell volume (V), x-ray density (ρ_x), and porosity (P) were determined using XRD data. The lattice constant (a), x-ray density (ρ_x) and porosity (P) decrease with an increase in Fe content x. The average particle size was calculated by using the Debye–Scherer's formula using XRD data and was 9–18 nm. The microstructural studies were investigated through scanning electron microscopy technique. Compositional stoichiometry was confirmed by energy dispersive spectrum analysis. The direct current electrical resistivity studies of the prepared samples were carried out in the temperature range of 343–1133 K using a standard two-probe method. The electrical conductivity (σ) increases with temperature and Fe concentration. The dielectric parameters such as dielectric constant (ε') and loss tangent (tan δ) were measured with frequency at room temperature in the frequency range 50 Hz to 5 MHz. The dielectric parameters show strong compositional as well as frequency dependences. The dielectric parameters were found to be higher at lower frequency.

Key words: Nanoceramics, perovskite, sol–gel, structural, electrical, dielectrical

INTRODUCTION

Perovskite structured ceramic materials with general chemical formula ABO_3 are value-added materials used for several applications such as capacitors, non-volatile memories, actuators and sensors, piezoelectric, ultrasonic and underwater devices, high temperature heating applications, frequency filters for wireless communications, *etc*.[1–5] They possess some peculiar properties viz. ferroelectric, thermo-electric, pyroelectric, dielectrical and optical properties.[6–8]

The alkaline-earth metal zirconates having the general chemical formula $AZrO_3$ (where, A-Ba, Sr, Ca) have been attractive as prominent structural and electronic ceramics.[9] Barium zirconate ($BaZrO_3$) is of great industrial and technological interest due to its attractive characteristics like high melting point (2920°C), poor thermal conductivity, excellent mechanical and structural integrity under extreme thermal conditions, high protonic conductivity, and pyroelectric properties.[10–15] Also, the high dielectric constant and low loss characteristics in $BaZrO_3$ ceramics make it as a promising material for various microwave applications.[16]

The proton conducting characteristics of yttrium doped barium zirconate is of great interest for a variety of electrochemical devices and solid oxide fuel cell (SOFC) applications.[14] High temperature proton conductors (HTPCs) have received increasing attention as alternative electrolyte materials for SOFCs over the past few decades.

(Received December 18, 2015; accepted March 19, 2016; published online March 30, 2016)

Recently, mixed ionic-electronic conductors having a perovskite structure with one or more cations in suitable doped form have been granted as an excellent ionic conductor. The doping of trivalent metal cations like Y^{3+} and Fe^{3+} with disparate valencies in $BaZrO_3$ provides either extra oxygen atoms when doped at the A-site or, oxygen vacancies when doped at the B-site. Both these conditions lead to creation of holes or electrons, causing electronic and ionic conductivity.[17]

Fe-doped $BaZrO_3$ is a candidate material for achieving high catalytic activity, material stability and oxygen permeability in various atmospheres at high temperatures. The doping of 3*d* to 5*d* transition metal atoms at B-site cations in perovskite oxides with a relatively large band gap (such as $BaTiO_3$, $BaZrO_3$) leads to electronic and ionic conductivities, usually attributed to a hopping conduction along the B–O–B bonding.[18] The small polaron hopping conductivity is apparently influenced considerably by a carrier formation mechanism due to the variation of the valence state (or redox state) of both the matrix and dopant cation and an electro-negativity of BO_6 octahedra.[19]

It is a well known fact that the properties of ceramic materials depend on their crystal structure, particle morphology and purity of the precursors. Nanoparticles with properties that diverge from those of bulk counterparts, such as high surface to volume ratio, have high surface energy that has been used in the preparation of ceramic materials permitting achievement of very homogenous microstructures and small grains at a low sintering temperature.[20]

In the literature, Fe doped $BaZrO_3$ ceramics have not been much reported. Zhang studied the electro-chemical and transport properties of $Ba_{0.90}Fe_{0.10}Zr_{0.90}O_{3-\delta}$ ceramics.[21] The electronic defect formation in Fe-Doped $BaZrO_3$ was studied via x-ray absorption spectroscopy by Kim.[22]

In this paper, we have reported detailed investigations on the sol–gel auto combustion synthesis, and structural, microstructural, broad temperature ranges electrical and frequency dependent dielectrical properties of $BaZr_{1-x}Fe_xO_3$ nanoceramics with various compositions, i.e., x = 0.0, 0.05, 0.10, 0.20, 0.30, 0.40 and 0.50.

EXPERIMENTAL

Materials

Analytical grade barium nitrate hexahydrate ($Ba(NO_3)_2{\cdot}6H_2O$, 99%, Merck), zirconyl nitrate hydrate ($ZrO(NO_3)_2{\cdot}H_2O$, 99.9%, Merck), ferric nitrate nonahydrate ($Fe(NO_3)_3{\cdot}9H_2O$, 99%, Merck), citric acid ($C_6H_8O_7$, 99.57%, Merck) and ammonium hydroxide (NH_4OH, 99%, Merck) were used without further purification.

Synthesis of $Ba_{1-x}Sr_xZrO_3$ Nanoceramics

$BaZr_{1-x}Fe_xO_3$ nanoceramics with composition x = 0.0, 0.05, 0.10, 0.20, 0.30, 0.40 and 0.50 were synthesized using the sol–gel auto combustion technique. The analytical grade barium nitrate, zirconyl oxynitrate, ferric nitrate, and citric acid were used as raw materials. According to the principles used in propellant chemistry, the oxidizing and reducing valencies of various elements, the metal nitrate to citric acid molar ratio was taken as 1:2. The salt solutions were mixed, and the resultant mixture was subjected to continuous stirring and heating at 80–90°C. Then, the ammonia solution was added drop-wise to maintain pH 7. Continuous heating of 110°C initiates the gel formation. Under constant stirring and heating, viscous gel transforms into dry gel. The auto catalytic nature of the combustion process of nitrate–citrate gel was studied, and the experimental observations showed that the dried gel formed from metal nitrates and citric acid exhibited self-propagating combustion behavior, and the entire combustion process was done in a few minutes. The obtained powders were dried, crushed and were annealed at 900°C for 5 h in a muffle furnace in order to obtain the nanocrystalline powders.

Characterizations

Crystalline phase of the samples was examined by a x-ray diffraction (XRD) pattern obtained using a PANalytical X'pert pro difractometer (Philips PW3373/10) at room temperature. The pattern was recorded using Cu-Kα radiation (λ = 1.54182 Å) in the 2θ range 20°–80° with step size 0.01° and time/step 2 s. The surface morphology and an average grain size of the prepared samples were determined by scanning electron microscopy (SEM) using a type field emission gun scanning electron microscope (Hitachi Model-S-4800) operated at 15 kV. The elemental analysis was carried out by using energy dispersive x-ray analysis (EDS) attached to SEM. The powders were mixed with a polyvinyl alcohol (PVA) agent as binder and pressed into cylindrical pellets with 10-mm diameter and 3-mm thickness under the pressure of 50 MPa. The pellets were sintered in a muffle furnace at 500°C for 2 h for removal of binder and used for bulk density, electrical and dielectrical measurements. The pellets were polished for smooth parallel faces and coated with silver paste to ensure good ohmic contact. Using the standard two-probe method, the direct current (DC) electrical conductivity of all samples was calculated. The dielectric properties of all the samples were measured using the LCR-Q meter (Hioki 3532-50, Japan) as a function of frequencies.

RESULTS AND DISCUSSION

X-ray Diffraction (XRD) and Structural Analysis

XRD patterns for all the synthesized samples are shown in Fig. 1. For all the samples, all the observed diffraction peaks can be indexed to the cubic perovskite structure with a very small amount of barium carbonate impurity phases. The peak position of the $BaZrO_3$ phase agrees well with standard data (JCPDS: 06-0399) that has a *Pm3m* space group.[23] The vertical bars on base in Fig. 1 are the standard peak positions reported in JCPDS data. The XRD data suggest that all the patterns are identical to standard phase and no secondary phases are found even though the doping concentration of Fe was up to 50%. Even if the high doping concentration can make sufficient oxygen vacancies, only cubic products are obtained. However, the decrease in peak intensity is observed for higher Fe content (x = 0.30, 0.40 and 0.50) that might also imply a decrease in the extent of crystallinity of the samples. The XRD patterns show that the peak positions (2θ) remain the same, but with decreasing intensity suggesting there is no change in the crystal lattice structure, which affirms its stability.

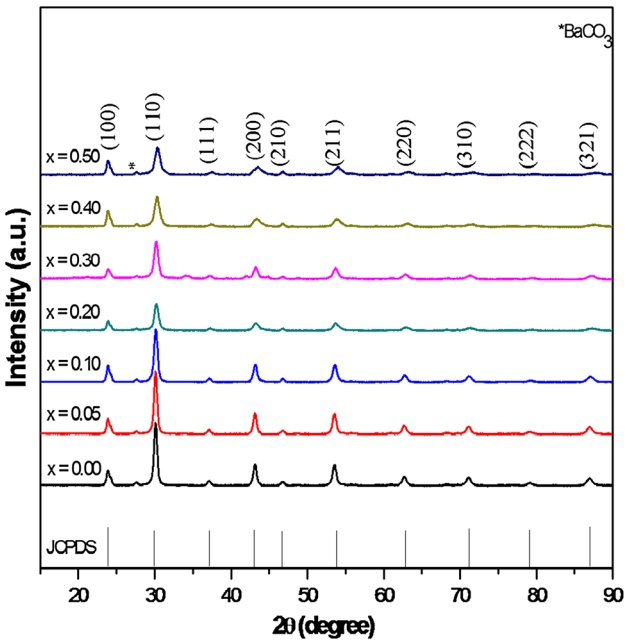

Fig. 1. X-ray diffraction patterns of $BaZr_xFe_{1-x}O_3$ (x = 0.0 – 0.50) ceramics (recorded at room temperature).

The lattice constant (a) of the prepared nanoceramics was determined from x-ray data analysis with an accuracy of ±0.002 Å using relations (1);

$$\frac{1}{d^2} = \frac{h^2 + k^2 + l^2}{a^2}, \quad (1)$$

where, a is the lattice constant, d is interplanar spacing and (hkl) are Miller indices. For pure $BaZrO_3$, the lattice constant was found to be a = 4.1930 Å, which is in a good agreement with the literature.[24]

The values of lattice parameters calculated using above equations are presented in the Table I. It is evident from Table 1 that the lattice constant (a) decreases as Fe concentration x increases in $BaZr_{1-x}Fe_xO_3$. This may be due to the lower ionic radii of Fe (0.645 Å) than that of zirconium (0.72 Å) obeying Vegard's law.[25] The variation of a with composition x is shown in Fig. 2.

The unit cell volume (V) is the most basic characteristic of the solid-state structure. The values of the unit cell volume are given in Table I. The volume of pure $BaZrO_3$ is greater than that of Fe doped $BaZrO_3$, and one might expect a simple linear change in the volume as the Fe fraction is increased.

The other structural parameters such as x-ray density (ρ_x), bulk density (ρ_B) and porosity (P%) were calculated using the relations (2), (3) and (4), respectively, and their values are given in Table I.

$$\rho_x = \frac{ZM}{N_A V}, \quad (2)$$

where, Z is the number of formula units in the unit cell (Z = 1), M is the molecular mass of the sample and N_A is Avogadro's number. X-ray density decreases with increase in Fe concentration of 6.2285–5.9660 g/cm^3.

The bulk density (ρ_B) of the pellets was measured using Archimedes method using water as solvent (ρ = 0.997 g/cm^3) and using the following equation.[26]

Table I. Lattice constant (a), unit cell volume (V), x-ray density (ρ_x), bulk density (ρ_B), porosity (P%), tolerance factor (t') and average crystallite size (t) of $BaZr_{1-x}Fe_xO_3$ nanoceramics (x = 0.0–0.5)

x	a (Å)	V (Å^3)	ρ_x (g/cm^3)	ρ_B (g/cm^3)	P (%)	t'	t (nm)
0.00	4.1930	73.7182	6.2285	5.2123	16.32	1.0113	18.09
0.05	4.1927	73.7024	6.1899	5.2099	15.83	1.0131	16.28
0.10	4.1889	73.5021	6.1668	5.1987	15.70	1.0150	14.13
0.20	4.1804	73.0556	6.1241	5.1931	15.20	1.0187	11.72
0.30	4.1775	72.9037	6.0563	5.1732	14.58	1.0224	11.34
0.40	4.1652	72.2616	6.0288	5.1687	14.27	1.0262	10.01
0.50	4.1609	72.0380	5.9660	5.1478	13.72	1.0299	9.26

$$\rho_B = \frac{W_{dry}}{W_{wet} - W_{sus}} \times d_{H_2O}, \quad (3)$$

where, W_{wet} and W_{dry} are wet and dry weights of the pellets subsequently measured in the air before and after drying at 100°C for 24 h, W_{sus} is the suspended weight in water of each pellet. The bulk density values were lower as compared to x-ray density, and its lower value is attributed to the pore formation during synthesis processes. The values of ρ_x and, ρ_B were used to obtain percentage porosity of all the samples;

$$P = 1 - \frac{\rho_B}{\rho_x}, \quad (4)$$

where, ρ_B is the bulk density and ρ_x is the x-ray density. The porosity of the present samples varies between 13% and 16%.

The average crystallite size (t) was calculated using the Debye–Scherrer's formula taking (110) plane of maximum intensity;

$$t = \frac{0.9\lambda}{\beta\cos\theta}, \quad (5)$$

where, λ is the wavelength of the Cu-Kα radiation, β is the full width of the half maximum and θ is the Bragg's angle. The average crystallite size (t) was found to be in the range of 9–18 nm (Table I). The decrease in t can be attributed to a decrease in a and V of the samples.

The prediction criteria for identification of formability of perovskite structure can be estimated by the calculating tolerance factor (t') suggested by Goldschmidt as[4];

$$t' = \frac{(r_A + r_O)}{\sqrt{2} \cdot (r_B + r_O)}, \quad (6)$$

where, r_A and r_B are the ionic radii of the A and B cations and r_O is the ionic radius of the oxygen anion (in Å units). For calculating the tolerance factor, the Shannon's ionic radii of Ba (1.61 Å), Fe (0.645 Å), Zr (0.72 Å) and O (1.35 Å) were taken.[27] The tolerance factor (t') was found to be in the range of 1.0113–1.0299, confirming the perovskite structure.[28] The variation of t' with Fe concentration x is shown in Fig. 2. The increase in the t' can be attributed to replacement of Zr by lower ionic radii Fe.

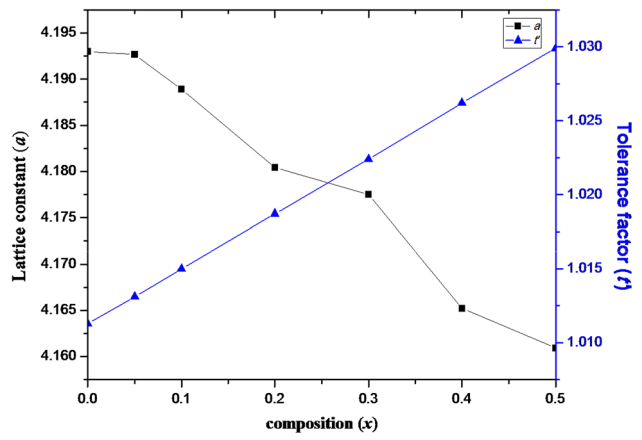

Fig. 2. Variation of lattice constant (a) and tolerance factor (t') with Fe composition x.

Microstructural and Compositional analysis

Microstructures and morphologies of the samples were observed by SEM. The representative SEM image of the sample x = 0.0 and 0.50 is shown in Fig. 3a and b respectively, which indicates dense nanoparticles surfaces and the well distributed crystallites. Samples have the large number of pores among the grains. Using the SEM images, the average grain size (G) was estimated from the linear intercept method for all the samples[29] and their values are given in Table II. An average grain size of pure barium zirconate samples was of the order of 96.25 nm, which decreases after Fe doping. The SEM micrographs agree with the results

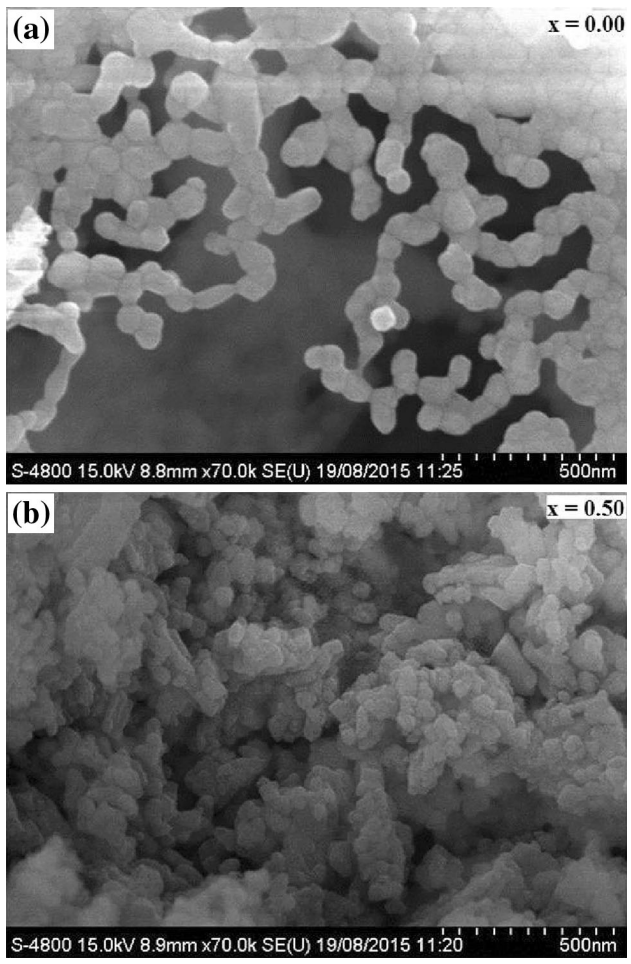

Fig. 3. SEM images of (a) $BaZrO_3$ and (b) $BaZr_{0.50}Fe_{0.50}O_3$ nanoceramics.

Table II. Average grain size (G) (from SEM), elemental weight percentage (wt.%) and atomic percentage (at.%) (from EDS) of $BaZr_{1-x}Fe_xO_3$ nanoceramics (x = 0.0–0.5)

		Ba		Zr		Fe		O	
x	G (nm)	wt.%	at.%	wt.%	at.%	wt.%	at.%	wt.%	at.%
0.00	96.25	44.71	12.52	22.92	9.66	–	–	32.37	77.82
0.05	74.43	47.80	16.05	27.54	13.92	0.52	0.43	24.14	69.60
0.10	68.69	49.86	17.13	25.69	13.29	1.21	1.01	23.24	68.57
0.20	62.15	49.53	16.85	24.33	12.46	2.72	2.27	23.42	68.42
0.30	54.76	49.23	16.80	21.52	11.06	6.46	5.41	22.79	66.73
0.40	31.71	48.70	16.62	17.34	8.90	11.97	10.04	21.99	64.44
0.50	21.30	48.30	17.64	16.98	9.33	16.02	14.38	18.70	58.65

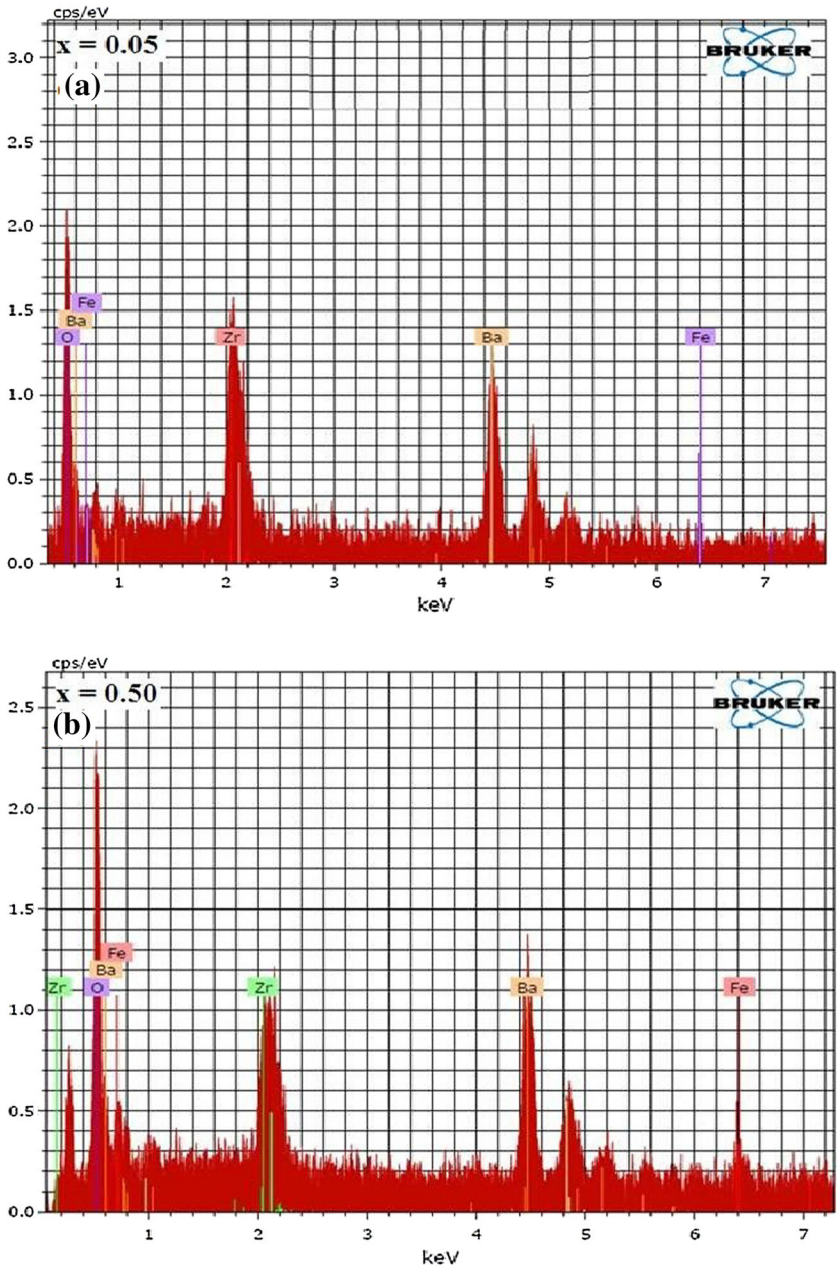

Fig. 4. EDS spectra of (a) $BaZr_{0.95}Fe_{0.05}O_3$ and (b) $BaZr_{0.50}Fe_{0.50}O_3$ nanoceramics.

calculated by the Debye–Scherrer's relation used for estimation of average crystallite size.

EDS patterns of $BaZr_{1-x}Fe_xO_3$ nanoceramics with composition $x = 0.05$ and 0.50 are shown in Fig. 4a and b, respectively. As was expected, the Fe concentration is highest for the $x = 0.50$ sample. As Fe doping increases, the percentage of Zr decreases. Table II gives the elemental weight percentage (wt.%) and atomic percentage (at.%) of Fe doped $BaZrO_3$ nanoceramics. In the EDS patterns are confirmed the presence of Ba^{2+}, Zr^{4+}, Fe^{3+} and O^{2-} elements in the proper proportions suggesting that the expected stoichiometry was maintained in the prepared samples with an error of 1–2%. The EDS results also confirmed that the precursors used for the synthesis have fully undergone the chemical reaction to form the required perovskite structured $BaZr_{1-x}Fe_xO_3$ nanoceramics.

DC Electrical Conductivity

The DC electrical conductivity studies of the prepared $BaZr_{1-x}Fe_xO_3$ nanoceramics ($x = 0.0$, 0.05, 0.10, 0.20, 0.30, 0.40 and 0.50) samples were carried out in the temperature range of 343–1133 K. The resistance for each sample at the same temperature was noted. The conductivity of doped $BaZrO_3$ was reported by several researchers and its value varies widely, from 1×10^{-6} S/cm lower value to 1×10^{-2} S/cm higher value near 600°C.[13,30–38] In early 1990, it was suggested that doped $BaZrO_3$ exhibits poor proton conductivity as compared to doped barium cerate. However, their reported data is still a controversial issue because these values differ by two orders of magnitude.[39] In 1999, Kreur reported the conductivity of Y^{3+} doped $BaZrO_3$ to be 5×10^{-5} S/cm at around 140°C, and the work was supported by Bohn and Schober.[40,41]

Figure 5 shows the variation of resistance (Log R) with temperature (T) for of $BaZr_xFe_{1-x}O_3$($x = 0.0$–0.50) nanoceramics. The variation of resistance (R) with temperature shows a decreasing trend with increasing temperature, revealing the semiconducting nature (850–1150 K) of the prepared ceramics. As the Fe concentration increases, the resistance decreases significantly. The sample of pure $BaZrO_3$ shows a highly resistive nature at low temperature. It is evident from Fig. 5 that the resistance decreases with increasing temperature, obeying the Arrhenius relation.[42] This confirms the semiconducting behaviour and single ionic conductor of Fe substituted $BaZrO_3$ samples under investigation.

The conductivity for each sample at the same temperature was calculated by using the equation below;

$$\sigma = \frac{l}{RA}, \tag{7}$$

where, l is the length of the pellet, R is the electrical resistance of a uniform specimen of the material (measured in ohms, Ω) and A is the cross-sectional area of the pellet.

The DC electrical conductivity (log σ) of the sample as a function of temperature as well as doping concentration is plotted in Fig. 6. It can be observed from Fig. 6 that the conductivity of each sample overall increases with the increase in temperature. The conductivity of all the samples was found to be highest in the temperature range 1000–1050 K. As Fe concentration increases, the conductivity increases drastically. The temperature of maximum conductivity (T_{max}) for the $x = 0.5$ sample is around 1020–1066 K and was found to be 1.344×10^{-3} S/cm. The initial linear increase in conductivity as a function of temperature is due to the oxygen vacancies, which act as a mobile charge species, creating free electrons.

The limited conductivity in lower Fe content ($x = 0.0$, 0.05 and 0.10) samples even at high temperature can be due to its refractory nature, leading to sintered samples with greater average grain size, high grain boundaries densities and low charge carrier species. As a consequence, the large electrical resistivity of the interfaces results in a material with low total electrical conductivity. The results on electrical conductivity are analogous to that of Sc doped $BaZrO_3$ reported in the literature.[43]

Dielectrical Studies

Dielectric properties of $BaZr_{1-x}Fe_xO_3$ nanoceramics ($x = 0.0$, 0.05, 0.10, 0.20, 0.30, 0.40 and 0.50) were studied at room temperature using a multi frequency LCR-Q meter. The capacitance (C) and loss tangent (tan δ) were measured in the frequency range 50 Hz to 5 MHz. Figures 7 and 8, respectively, show the variation of dielectric constant (ε') and loss tangent (tan δ) as a function of frequency at room temperature as well as Fe concentration x.

The dielectric constant (ε') was calculated using the formula[44]:

$$\varepsilon' = \frac{Ct}{\varepsilon_0 A}, \tag{8}$$

where, C is the capacitance of a pellet, t is the thickness of the specimen, A is the area of a cross section of the pellet, and ε_0 is the permittivity of the free space.

The dependence of dielectric constant with frequency is shown in Fig. 7. It is observed that the dielectric constant is high in the range of low frequency, and it decreases with frequency. The reasons for the high value of the dielectric constant at low frequencies may be due to dislocations, vacancies like oxygen, voids and defects present in the crystal structure of nanoceramics. The decrease in ε' with increasing frequency is due to the fact that the electrical dipoles in the samples do not show a response to the increasing frequency because some of the dipoles cannot be timely polarized following

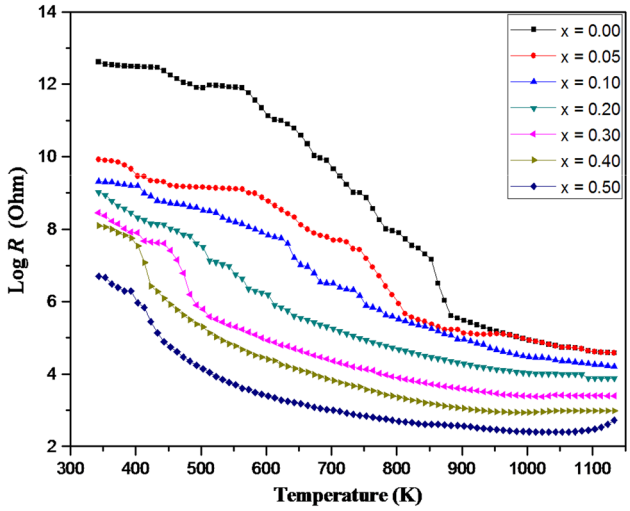

Fig. 5. Variation of resistance (Log R) with temperature (T) for $BaZr_xFe_{1-x}O_3$(x = 0.0–0.50) nanoceramics (Color figure online).

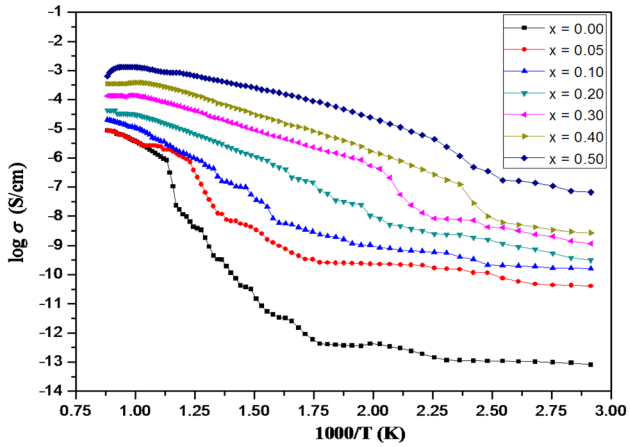

Fig. 6. Arrhenius plots of the total electrical conductivity (Log σ in S/cm) for $BaZr_xFe_{1-x}O_3$(x = 0.0–0.50) nanoceramics (Color figure online).

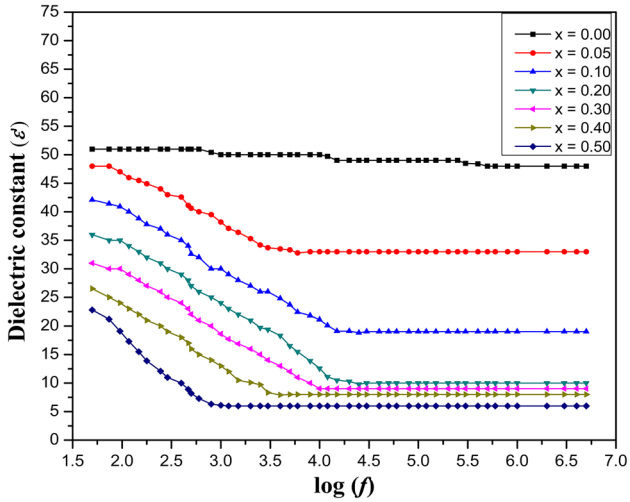

Fig. 7. Variation of dielectric constant (ε') with frequency at room temperature of $BaZr_xFe_{1-x}O_3$ (x = 0.0–0.50) nanoceramics (Color figure online).

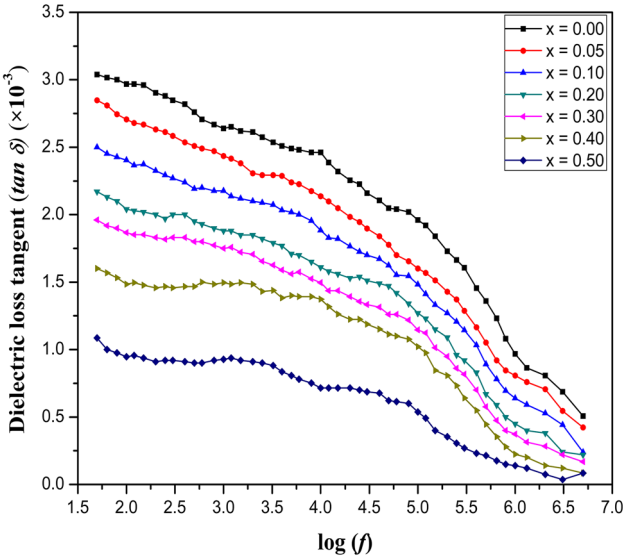

Fig. 8. Variation of dielectric loss tangent (tan δ) with frequency at room temperature of $BaZr_xFe_{1-x}O_3$ (x = 0.0–0.50) nanoceramics (Color figure online).

the fast change in electric field. When the frequency is increased beyond a certain frequency limit, the electron hopping cannot follow the electric field fluctuations and causes a decrease in the dielectric constant. At high frequencies the value of the dielectric constant is low because it comes from the grains having a small value of dielectric constant due to low resistivity and becomes less dependent on frequency. The dielectric constant of pure $BaZrO_3$ is found to be $\varepsilon' = 51$, which is relatively high, and it remains high even at higher frequencies which are suitable for microwave applications. Figure 8 shows the variation of tan δ as a function of frequency. For pure $BaZrO_3$, tan δ is found to be 3.04×10^{-3} at 50 Hz frequency, however, at 5 MHz it is found to be 0.507×10^{-3}.

Figures 7 and 8 also show variation of ε' and tan δ with a Fe doping concentration in $BaZrO_3$. It can be observed that both ε' and *tan* δ values decrease with increase in Fe concentration. The mechanism of electrical conduction in $BaZrO_3$-based semiconductors is analogous to dielectric polarization. At lower Fe concentrations, the hopping mechanism between Fe^{3+} and Fe^{4+} ions, which are replacing Ti^{4+} ions, is predominant which results in a higher value of ε' and tan δ values.

As the doping concentrations of Fe increase, the Fe^{3+} ion substituting Ti^{4+} can behave as a deep electron donor, which will give rise to the electrical conductivity and, therefore, a reduction in the ε' and tan δ values. The dielectrical properties of ceramic materials also depend on density and porosity.[45] It is also clear from the porosity values (Table 1) of Fe doped samples that they exhibit high porosity and, hence, ε' and tan δ have lower values. Overall, as the frequency and Fe concentration increases, the material approaches a relaxation point, the

dielectric loss factor (and hence conductivity) increases, and this corresponds to a decrease in dielectric constant. The obtained results on pure $BaZrO_3$ are in good agreement with the literature reports.[46,47]

CONCLUSIONS

We have synthesized $BaZr_{1-x}Fe_xO_3$ (x = 0.0, 0.05, 0.10, 0.20, 0.30, 0.40 and 0.50) nanoceramics by the sol–gel auto combustion method. All the samples are identical with cubic perovskite structure analyzed by XRD. Fe doping did not change the lattice structure of the material, but formed a homogeneous single cubic perovskite structure. The lattice constant has been observed to decrease linearly with Fe doping obeying Vegard's law. The average crystallite size goes on decreasing with Fe concentration. The bulk density was quite low as compared to x-ray density. SEM revealed that the particles are aggregated in spherical shape and in the nanometer range. EDS analysis confirmed that the synthesized samples were near stoichiometries. The resistance decreases as temperature increases showing the semiconducting nature of the prepared samples in the temperature range 850–1100 K. Through a series of defect reactions, the role of Fe doping and the mechanism for the enhancement of conductivity caused by Fe doping were clarified. Samples carrier concentrations were increased by Fe dopants. As a result, the conductivity of samples increased. After all, the sample x = 0.50 had the highest conductivity of 1.344×10^{-3} S/cm tested near 1046 K. The dielectric behavior shows strong frequency as well as composition dependence. The dielectric constant and dielectric loss tangent both decrease linearly with an increase in frequency. As the Fe doping level increases, dielectric constant and dielectric loss tangent decrease significantly. At lower frequencies, it is observed that the dielectric properties are high.

ACKNOWLEDGEMENT

The author Mr. Pankaj P. Khirade is very much thankful to Department of Physics, IIT Mumbai for providing X-ray diffraction (XRD) and North Maharashtra University, Jalgaon, for scanning electron microscopy (SEM) characterization facilities.

REFERENCES

1. Z.Y. Wu, C.B. Ma, X.G. Tang, R. Li, Q.X. Liu, and B.T. Chen, *Nanoscale Res. Lett.* 8, 207 (2013).
2. X. Jia, H. Fan, X. Lou, and J. Xu, *Appl. Phys. A* 94, 837 (2009).
3. B. Praveenkumar, H.H. Kumar, and D.K. Kharat, *Bull. Mater. Sci.* 28, 453 (2005).
4. S. Yamanaka, K. Kurosaki, T. Maekawa, T. Matsuda, S.I. Kobayashi, and M. Uno, *J. Nucl. Mater.* 344, 61 (2005).
5. N. Setter, D. Damjanovic, L. Eng, G. Fox, S. Gevorgian, S. Hong, A. Kingon, H. Kohlstedt, N.Y. Park, G.B. Stephenson, I. Stolitchnov, A.K. Taganstev, D.V. Taylor, T. Yamada, and S. Streiffer, *J. Appl. Phys.* 100, 051606 (2006).
6. Y. Xu, *Ferroelectric Materials and Their Applications* (Amsterdam: North-Holland, 1991).
7. R.V.K. Mangalam, N. Ray, U.V. Waghmare, A. Sundaresan, and C.N.R. Rao, *Solid State Commun.* 149, 1 (2009).
8. Y. Guo, M. Lia, W. Zhao, D. Akai, K. Sawada, M. Ishida, and M. Gu, *Thin Solid Films* 517, 2974 (2009).
9. W. Zając, D. Rusinek, K. Zheng, and J. Molenda, *Cent. Eur. J. Chem.* 11, 471 (2013).
10. S. Parida, S.K. Rout, L.S. Cavalcante, E. Sinha, M. Siu Li, V. Subramanian, N. Gupta, V.R. Gupta, J.A. Varela, and E. Longo, *Ceram. Int.* 38, 2129 (2012).
11. R. Vassen, X. Cao, F. Tietz, D. Basu, and D. Stover, *J. Am. Ceram. Soc.* 83, 2023 (2000).
12. P.G. Sundell, M.E. Bjorketun, and G. Wahnstrom, *Phys. Rev. B* 73, 104112 (2006).
13. K.D. Kreuer, *Annu. Rev. Mater. Res.* 33, 333 (2003).
14. M.D. Gonçalves, P.S. Maram, R. Muccillo, and A. Navrotsky, *J. Mater. Chem. A* 2, 17840 (2014).
15. S. Yamanaka, T. Hamaguchi, T. Oyama, T. Matsuda, S.I. Kobayashi, and K. Kurosaki, *J. Alloys Compd.* 359, 1 (2003).
16. D. Ehre, V. Lyahovitskaya, A. Tagantsev, and I. Lubomirsky, *Adv. Mater.* 19, 1515 (2007).
17. M. Saiful Islam, P.R. Slater, J.R. Tolchard, and T. Dinges, *Dalton Trans.* 19, 3061 (2004).
18. E. Konysheva and J.T.S. Irvine, *Chem. Mater.* 23, 1841 (2011).
19. M. Abbate, F.M.F. De Groot, J.C. Fuggle, A. A.Fujimori, O. Strebel, F. Lopez, M. Domke, G. Kaindl, G.A. Sawatzky, M. Takano, and Y. Takeda, *Phys. Rev. B* 46, 4511 (1992).
20. P. Moriarty, *Rep. Prog. Phys.* 64, 297 (2001).
21. H. Zhang, A. Suresh, C.B. Carter, and B.A. Wilhite, *Solid State Ionics* 266, 58 (2014).
22. D.-Y. Kim, S. Miyoshi, T. Tsuchiya, and S. Yamaguchi, *Chem. Mater.* 26, 927 (2014).
23. R. Borja-Urbya, L.A. Díaz-Torresa, P. Salasb, E. Moctezumac, M. Vegad, and C. Ángeles-Cháveze, *Mater. Sci. Eng. B* 176, 1382 (2011).
24. K. Kanie, Y. Seino, M. Matsubara, M. Nakaya, and A. Muramatsu, *New J. Chem. (RSC)* 38, 3548 (2014).
25. L. Vegard, *Z. Phys.* 5, 17 (1921).
26. R. Pornprasertsuk, C. Yuwapttanawong, S. Permkittikul, and T. Tungtidtham, *Int. J. Precis. Eng. Manuf.* 13, 1813 (2012).
27. R.D. Shannon, *Acta Crystallogr. A* A32, 751 (1976).
28. M.A. Pena and J.L.G. Fierro, *Chem. Rev.* 101, 1981 (2001).
29. V. Pillai and D.O. Shah, *J. Magn. Magn. Mater.* 163, 243 (1996).
30. A. Manthiram, J.F. Kuo, and J.B. Goodenough, *Solid State Ionics* 62, 225 (1993).
31. R.C.T. Slade, S.D. Flint, and N. Singh, *Solid State Ionics* 82, 135 (1995).
32. K. Katahira, Y. Kohchi, T. Shimura, and H. Iwahara, *Solid State Ionics* 138, 91 (2000).
33. V.P. Gorelov, V.B. Balakireva, Y.N. Kleshchev, and V.P. Brusentsov, *Inorg. Mater.* 37, 535 (2001).
34. M. Laidoudi, I. Abu Talib, and R. Omar, *J. Phys. D Appl. Phys.* 35, 397 (2002).
35. F.M.M. Snijkers, A. Buekenhoudt, J. Cooymans, and J.J. Luyten, *Scr. Mater.* 50, 655 (2004).
36. W.S. Wang and A.V. Virkar, *J. Power Sources* 142, 1 (2005).
37. C.D. Savaniu, J. Canales-Vazquez, and J.T.S. Irvine, *J. Mater. Chem.* 15, 598 (2005).
38. F. Iguchi, T. Yamada, N. Sata, T. Tsurui, and H. Yugami, *Solid State Ionics* 177, 2381 (2006).
39. H. Iwahara, T. Yajima, T. Hibino, K. Ozaki, and H. Suzuki, *Solid State Ionics* 61, 65 (1993).
40. K.D. Kreuer, *Solid State Ionics* 125, 285 (1999).
41. H.G. Bohn and T. Schober, *J. Am. Ceram. Soc.* 83, 768 (2000).

42. Y.F. Qu, *Physical Properties of Functional Ceramics*, ed. Y.F. Qu (Beijing: Chemical Industry Press, 2007), p. 27.
43. R. Guo, L. Wu, J. Ren, J. Zhang, and H. Jiang, *Rare Met.* 31, 71 (2012).
44. V. Vinayak, P.P. Khirade, S.D. Birajdar, R.C. Alange, and K.M. Jadhav, *J. Supercond. Nov. Magn.* 28, 3351 (2015).
45. R.V. Mangalaraja, P. Manohar, and F.D. Gnanam, *J. Mater. Sci.* 39, 2037 (2004).
46. O.A. Al-Hartomy, M. Ubaidullah, D. Kumar, J.H. Madani, and T. Ahmad, *J. Mater. Res.* 28, 1070 (2013).
47. H. Padma Kumara, C. Vijayakumara, C.N. Georgeb, S. Solomonc, R. Josed, J.K. Thomasa, and J. Koshya, *J. Alloys Compd.* 458, 528 (2008).